Effects of nucleus orientation on transfer process and production of unknown neutron-rich isotopes with $Z = 62$–75 in ^{204}Hg + ^{232}Th based on the dinuclear system model

Xin-Rui Zhang,[1,2] Gen Zhang,[3] Jing-Jing Li,[2] Shi-Hui Cheng,[1,2] Zhong Liu,[4] and Feng-Shou Zhang[1,2,5,*]

[1]*The Key Laboratory of Beam Technology and Material Modification of Ministry of Education, College of Nuclear Science and Technology, Beijing Normal University, Beijing 100875, China*

[2]*Beijing Radiation Center, Beijing 100875, China*

[3]*School of Physical Science and Technology, Guangxi University, Nanning 530004, China*

[4]*Institute of Modern Physics, Chinese Academy of Sciences, Lanzhou 730000, China*

[5]*Center of Theoretical Nuclear Physics, National Laboratory of Heavy Ion Accelerator of Lanzhou, Lanzhou 730000, China*

(Received 18 November 2020; accepted 26 January 2021; published 16 February 2021)

Within the framework of the dinuclear system model, the contributions of the constituent parts of the driving potentials in different orientation configurations in the ^{86}Kr + ^{166}Er reaction are investigated. The Coulomb potential plays a predominant role in the change of driving potential among different configurations with mass number $A_1 = 52$–200. In the region of $A_1 < 52$ and $A_1 > 200$, the effects of the nuclear potential increased significantly. This work also studied the multinucleon transfer process of ^{204}Hg + ^{232}Th in tip-to-tip and side-to-side configurations to produce unknown neutron-rich isotopes with $Z = 62$–75. In the ^{204}Hg + ^{232}Th reaction, the tip-to-tip configuration accounts for the main contribution to produce unknown neutron-rich isotopes with $Z = 62$–75 because of the "inverse" quasifission process. The optimal incident energy is 678.1 MeV. Considering the experimental conditions provided by the experiments, there are 29 unknown isotopes whose production rate is greater than one count per day. Especially, the production rates per day of ^{179}Ho, ^{181,182}Er, ^{182,183,184}Tm, ^{186}Yb, ^{189}Lu, ^{191,192}Hf, and ^{195}Ta are 21, 25, 13, 701, 1217, 29, 94, 29, 102, 29, and 20, respectively. The reaction of ^{204}Hg + ^{232}Th at 678.1 MeV is a potential candidate to produce new neutron-rich nuclei with $Z = 62$–75.

DOI: 10.1103/PhysRevC.103.024608

I. INTRODUCTION

Up to now, the total number of observed nuclides is up to 3310 [1]. There are many undiscovered neutron-rich nuclei in the rare earth region. At present, the unknown nuclear properties of some neutron-rich rare earth nuclei are essential inputs for the theoretical calculations of the prediction of the r-process, which leads to high uncertainty of the results [2]. Also, the properties of nuclei around the peak with mass number A = 195 ($Z \approx 70$) of solar abundance distribution are still unknown, which is urgently needed to study the evolution of magic numbers far away from the β stability line [3].

To enrich the nuclear map toward the neutron drip-line is one of the most primary tasks in current nuclear physics. But under the current experimental equipment and the technic conditions, experiments for producing neutron-rich nuclei in this region are incredibly scarce, because of the extremely low cross sections provided in the projectile fragmentation process and the lack of appropriate neutron-rich projectiles and targets in the fusion process. For producing the neutron-rich rare earth nuclei, the in-flight fission of ^{238}U beam impinged on ^{9}Be target were performed at the RIKEN [4] and GSI [5], the incident energy are 345 MeV/nucleon and 1 GeV/nucleon, respectively. Both experiments produced a large number of isotopes; however, the production cross sections are at the level of pb when the charge number is close to 70.

The multinucleon transfer reaction (MNT) has arisen as one promising method to produce neutron-rich nuclei far from stability. Many neutron-rich nuclei with the charge number $Z \approx 70$ was produced in MNT reactions many years ago [6–9]. In recent years, great achievements have been made in the production of new exotic isotopes experimentally [3,10–29]. Various models can well describe the multinucleon transfer process in low-energy heavy-ion collisions. The models include dinuclear system (DNS) model [30–35], GRAZING model [36–39], the Langevin equations [40–42], the time-dependent Hartree-Fock (TDHF) model [43–50] and improved quantum molecular dynamics (ImQMD) model [51–53], etc. For a thorough review, see Refs. [54–60].

In recent years, the quasifission process in MNT reactions around the Coulomb barrier has aroused great interest among researchers, especially the "inverse" quasifission process (nucleons mainly transfer from the lighter partner to the heavy one) [61–64]. As we have known, the proportion of quasifission is considerable when the total mass number is higher than 230 [65], and the impact of the shell effects on quasifission is clearly visible [66–68]. For more symmetrical reaction systems, the shell effects may lead to the inverse quasifission process, of which the production cross sections of neutron-rich nuclei may increases obviously [62,64]. Back in 2007,

*Corresponding author: fszhang@bnu.edu.cn

Zagrebaev predicted that the ^{160}Gd + ^{186}W reaction near the Coulomb barrier is an "inverse" quasifission process based on the Langevin-type equations [62]. In 2017, the experiment confirmed this prediction and found increased yields in the trans-target fragments [64]. It worth mentioning that the DNS model describes the experimental results of the ^{160}Gd + ^{186}W reaction well [69].

This paper will study the MNT reaction of ^{204}Hg + ^{232}Th to produce new neutron-rich isotopes with the charge number $Z \approx 70$ by using the DNS model. Many neutron-rich nuclei have large deformation. They are in various orientations before reaching the contact configuration, and the orientation effects have a strong influence on the reaction process [42,64,70]. Therefore, this work will investigate the contribution of the constituent parts of driving potential in different orientations and study orientation effects on the multinucleon transfer process around the Coulomb barrier.

The article is organized as follows. In Sec. II, we briefly introduce the DNS model. The results and discussion are presented in Sec. III. Finally, we give a conclusion in Sec. IV.

II. THE MODEL

A. The potential energy surface

In the DNS model, the potential energy surface (PES) [71,72] plays a crucial role in the nucleon transfer process, and it is defined as

$$U(Z_1, N_1, \theta_1, \theta_2, R_{\rm cont}) = \Delta(Z_1, N_1) + \Delta(Z_2, N_2) + V_{\rm CN}(Z_1, N_1, \theta_1, \theta_2, R_{\rm cont}). \quad (1)$$

Here, $\Delta(Z_i, N_i)$ $(i = 1, 2)$ is mass excess of the two fragments, Z_i, N_i denotes proton number and neutron number of the ith fragments, respectively. The sum of Z_1 and Z_2 is the total number of protons of the composite system. The situation of neutrons is the same. $V_{\rm CN}(Z_1, N_1, \theta_1, \theta_2, R_{\rm cont})$ is the effective nucleus-nucleus interaction potential between the two fragments, θ_i is the angle between the symmetry axis of fragment i and the collision axis, see Fig. 1(a), this figure is the schematic diagram of the orientation configuration of two prolately deformed colliding nuclei. $R_{\rm cont}$ is the location of potential pocket when the nucleus-nucleus potential contains a potential pocket; otherwise, it can be obtained with the equation $R_{\rm cont} = R_1[1 + \beta_2^{(1)}Y_{20}(\theta_1)] + R_2[1 + \beta_2^{(2)}Y_{20}(\theta_2)] +$ 0.7fm, $\beta_2^{(i)}$ $(i = 1, 2)$ is quadrupole deformation parameters of fragment i and taken from Ref. [73]. The mass excess can be shown as

$$\Delta(Z_i, N_i) = Z_i\Delta(^1H) + N_i\Delta(n) - a_{\rm v}(1 - \kappa I^2)A_i + a_{\rm s}(1 - \kappa I^2)A_i^{2/3} + a_{\rm c}Z_i^2/A_i^{1/3} - c_4Z_i^2/A_i - E_{\rm pair}(Z_i, N_i) + E_{\rm sh}(Z_i, N_i), \quad (2)$$

where the liquid drop parameters are $a_{\rm v} = 15.677$MeV, $a_{\rm s} =$ 18.56MeV, $a_{\rm c} = 0.717$MeV, $\kappa = 1.79$, and $c_4 = 1.211$MeV. $I = (N - Z)/A$ denotes the neutron-proton asymmetry of the fragment. The pair energy $E_{\rm pair}$ and the shell correction energy $E_{\rm sh}$ of the fragment listed in Ref. [73]. The effective nucleus-nucleus interaction potential between the two fragments can be expressed as

$$V_{\rm CN}(Z_1, N_1, \theta_1, \theta_2, R) = V_{\rm C}(Z_1, N_1, \theta_1, \theta_2, R) + V_{\rm N}(Z_1, N_1, \theta_1, \theta_2, R). \quad (3)$$

The Coulomb potential adopts wong's formula [74] by which the influence of deformation and orientation of two fragments is considered:

$$V_{\rm C}(Z_1, N_1, \theta_1, \theta_2, R) = \frac{Z_1Z_2e^2}{R} + \left(\frac{9}{20\pi}\right)^{1/2}\left(\frac{Z_1Z_2e^2}{R^3}\right) \times \sum_{i=1}^{2} R_i^2\beta_2^{(i)}P_2(\cos\theta_i) + \left(\frac{3}{7\pi}\right)\left(\frac{Z_1Z_2e^2}{R^3}\right) \times \sum_{i=1}^{2} R_i^2\left[\beta_2^{(i)}P_2(\cos\theta_i)\right]^2. \quad (4)$$

Here, R denotes the centroid distance between two nuclei, R_i is the nuclear radius of fragment i. The nuclear potential part using double folding potential [75],

$$V_{\rm N}(Z_1, N_1, \theta_1, \theta_2, R) = C_0\left\{\frac{F_{\rm in} - F_{\rm ex}}{\rho_0}\left[\int \rho_1^2(\mathbf{r})\rho_2(\mathbf{r} - \mathbf{R})d\mathbf{r} + \int \rho_1(\mathbf{r})\rho_2^2(\mathbf{r} - \mathbf{R})d\mathbf{r}\right] + F_{\rm ex}\int \rho_1(\mathbf{r})\rho_2(\mathbf{r} - \mathbf{R})d\mathbf{r}\right\}, \quad (5)$$

with

$$F_{\rm in} = f_{\rm in} + f'_{\rm in}\frac{N_1 - Z_1}{A_1}\frac{N_2 - Z_2}{A_2},$$
$$F_{\rm ex} = f_{\rm ex} + f'_{\rm ex}\frac{N_1 - Z_1}{A_1}\frac{N_2 - Z_2}{A_2}.$$

For the fixed value of constant $C_0 = 300$MeV fm^3, the values of the amplitudes were recommend in Ref. [76]: $f_{\rm in} =$

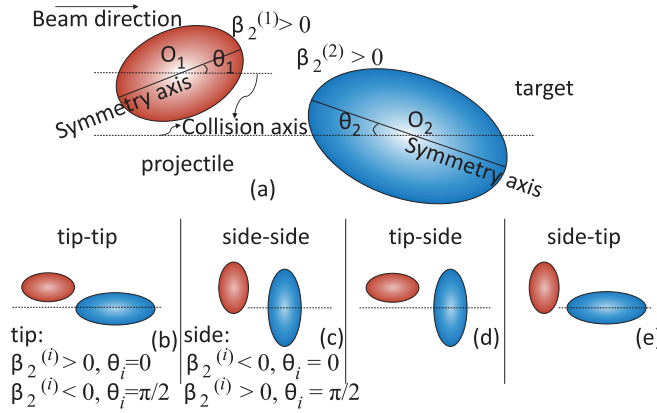

FIG. 1. (a) The schematic diagram of the orientation configurations of two prolately deformed colliding nuclei, $\beta_2^{(i)}$ $(i = 1, 2)$ is quadrupole deformation parameters. (b–e) The schematic diagram of tip-to-tip, side-to-side, tip-to-side, and side-to-tip collisions, respectively.

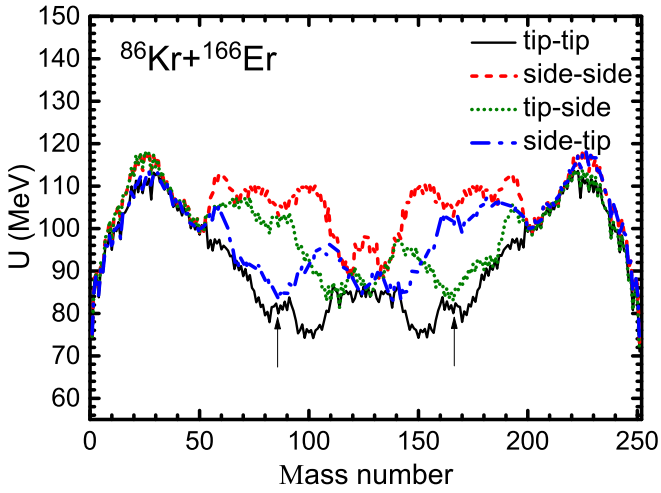

FIG. 2. The driving potential of the tip-to-tip (black solid line), side-to-side (red dashed line), tip-to-side (olive short dotted line), and side-to-tip (blue dash-dotted line) configurations in the reaction of $^{86}\mathrm{Kr} + ^{166}\mathrm{Er}$. The arrows indicate the injection points.

0.09, $f_{\mathrm{ex}} = -2.59$, $f'_{\mathrm{in}} = 0.42$, and $f'_{\mathrm{ex}} = 0.5$. ρ_0 denotes mean nuclear densities in the center of a composite system. $\rho_1(\mathbf{r})$ and $\rho_2(\mathbf{r} - \mathbf{R})$ are the density distribution of two nuclei, which are expressed as the Woods-Saxon form. In the DNS model, the shell corrections are included in the mass excess formulas to describe the properties of the individual nucleus. The nucleus-nucleus interaction potential V_{CN} does not include the additional microscopic shell correction terms, which still acts on the fragments in the transfer process of the DNS configuration. The shell effects that include microscopic terms for the binary configuration have been studied based on the deformed two-center shell model in Refs. [77,78].

There may be some particular distribution probabilities of orientations with all possible orientation configurations before reaching the contact configuration. We need to consider the distribution probabilities in our calculations for fully describing various nuclear reactions. Still, it is hard to do like that. In this paper, we discussed the orientation effects on the multinucleon transfer process based on four typical configurations. Let us briefly introduce the four particular orientation configurations firstly. Figures 1(b)–1(e) is the schematic diagrams of so-called tip-to-tip, side-to-side, tip-to-side, and side-to-tip orientation configurations, respectively. The value of θ_i corresponding to different orientations are shown in the left corner of Fig. 1, if $\beta_2^{(i)} > 0$, then $\theta_i = 0$ for tip orientation and $\theta_i = \pi/2$ for side orientation; otherwise, $\theta_i = \pi/2$ for tip orientation and $\theta_i = 0$ for side orientation.

The driving potential of these four configurations in $^{86}\mathrm{Kr} + ^{166}\mathrm{Er}$ are presented in Fig. 2. It is obvious that the driving potentials of tip-to-tip and side-to-side configurations are symmetric, and the Coulomb repulsion effects of side-to-side configuration are stronger than the tip-to-tip configuration. The arrows in Fig. 2 indicate the injection points, and one can see that the driving potential in side-to-side configuration has a smaller fluctuation near the entrance channel compared to that in the tip-to-tip configuration, this phenomenon caused an increase in the production cross sections of the nuclei

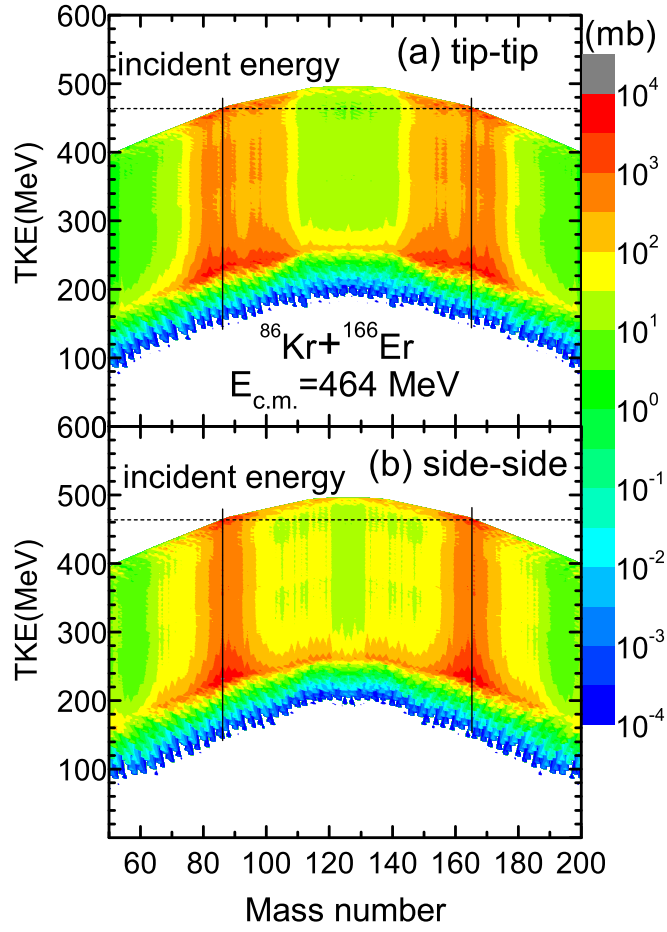

FIG. 3. The mass distribution of total kinetic energy of the primary binary fragments in the reaction of $^{86}\mathrm{Kr} + ^{166}\mathrm{Er}$ at $E_{\mathrm{c.m.}} = 464$ MeV, (a) and (b) denote tip-to-tip and side-to-side configurations, respectively; dashed and solid lines indicate bombarding energy and injection points, respectively.

slightly away from the projectile. Also, the injection points in this reaction are far from the Businaro-Gallone (BG) point, which is the highest point of the driving potential. So even in side-to-side configuration, the composite system easy to reseparate after transfer nucleons from one to another nucleus.

It can be observed very clearly in the mass distribution of total kinetic energy (TKE) of the primary binary fragments. The TKE with proton number Z_1 and neutron number N_1 can be calculated by

$$TKE(Z_1, N_1, \theta_1, \theta_2, \tau_{\mathrm{int}}) = E_{\mathrm{c.m.}} + Q_{\mathrm{gg}}(Z_1, N_1) - E^{\mathrm{diss}}(Z_1, N_1, \theta_1, \theta_2, \tau_{\mathrm{int}}). \quad (6)$$

Here, Q_{gg} is the ground-state reaction energy determined by the mass of projectile, target, projectilelike fragment (PLF), and targetlike fragment (TLF).

Figure 3 shows the TKE of the primary binary fragments in $^{86}\mathrm{Kr} + ^{166}\mathrm{Er}$, Figs. 3(a) and 3(b) corresponding to tip-to-tip and side-to-side configurations, respectively; dashed and solid lines indicate bombarding energy and projectile (or target), respectively. Both mass-TKE distributions have typical wide shape, but the fragments form after transferred more nucleons

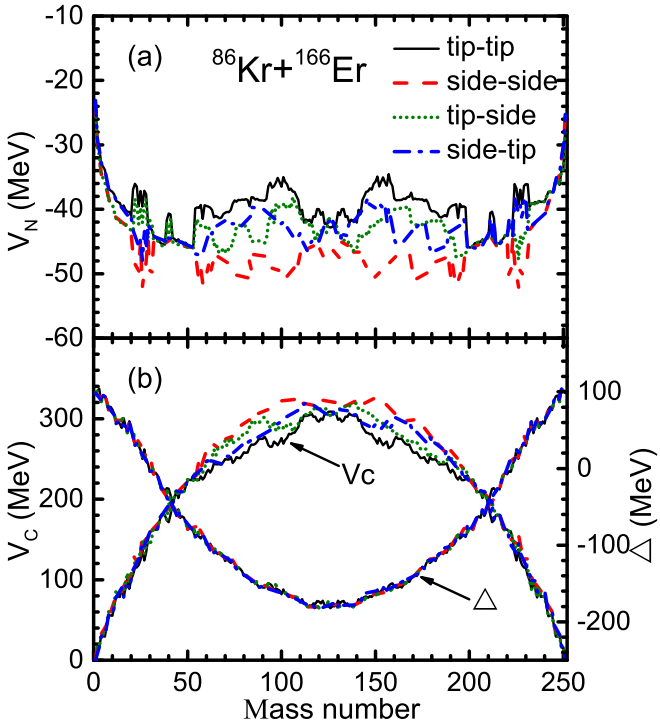

FIG. 4. (a) The nuclear potential. (b) The Coulomb potential and mass excess of four configurations in the reaction of $^{86}\mathrm{Kr} + {}^{166}\mathrm{Er}$.

in side-to-side configuration compared to tip-to-tip configuration. The driving potential of tip-to-side and side-to-tip configurations are between the tip-to-tip and side-to-side configurations, and symmetrical to each other. In the vicinity of the projectile, the driving potential of the tip-to-side configuration is close to that of the side-to-side configuration and the driving potential of the side-to-tip configuration is close to that of the tip-to-tip configuration.

The contributions of the constituent parts of the driving potentials in different orientations in the $^{86}\mathrm{Kr} + {}^{166}\mathrm{Er}$ reaction are studied. The nuclear potential, the Coulomb potential, and the mass excess (the sum of the mass excesses of PLF and TLF) of four typical configurations are shown in Figs. 4(a) and 4(b), respectively. The Coulomb potential and the mass excess vary widely as the mass number changes, with a range of about 300 MeV. By contrast, the range of the nuclear potential is minimal. From Fig. 4(a), we can see that the differences of the nuclear potential of the four configurations is pronounced, but the corresponding variation range is relatively small, about 20 MeV. And the Coulomb potential varies significantly among different orientation configurations with mass number $A_1 = 52$–200 ($A_1 = N_1 + Z_1$), where the maximum difference is nearing 60 MeV. However, the difference become very small in the region of $A_1 < 52$ and $A_1 > 200$, it is less than or equivalent to the change of the nuclear potential. This is due to the relatively small deformation of nuclei with mass number less than 52 (PLF or TLF). From Fig. 4(b), we can see that orientation effects have a small impact on the mass excess; the slight variation is caused indirectly by the changes of the Coulomb potential and the nuclear potential. In conclusion, the Coulomb potential plays a predominant role in the change of the driving potential among different orientation configurations with mass number $A_1 = 52$–200. But in the region of $A_1 < 52$ and $A_1 > 200$, the effects of the nuclear potential increased significantly.

B. The mass distribution probability

The mass distribution probability $P(Z_1, N_1, E_1, \theta_1, \theta_2, t)$ for fragment with Z_1 and N_1 can be obtained by solving the master equation [79]:

$$\begin{aligned}
&\frac{dP(Z_1, N_1, E_1, \theta_1, \theta_2, t)}{dt} \\
&= \sum_{Z_1'} W_{Z_1,N_1;Z_1',N_1}(t)\big[d_{Z_1,N_1}P(Z_1', N_1, E_1, \theta_1, \theta_2, t) \\
&\quad - d_{Z_1',N_1}P(Z_1, N_1, E_1, \theta_1, \theta_2, t)\big] \\
&\quad + \sum_{N_1'} W_{Z_1,N_1;Z_1,N_1'}(t)\big[d_{Z_1,N_1}P(Z_1, N_1', E_1, \theta_1, \theta_2, t) \\
&\quad - d_{Z_1,N_1'}P(Z_1, N_1, E_1, \theta_1, \theta_2, t)\big] - \{\Lambda_{\mathrm{qf}}[\Theta(t)] \\
&\quad + \Lambda_{\mathrm{fis}}[\Theta(t)]\}P(Z_1, N_1, E_1, \theta_1, \theta_2, t),
\end{aligned} \tag{7}$$

$W_{Z_1,N_1;Z_1',N_1}(t)$ and $W_{Z_1,N_1;Z_1,N_1'}(t)$ is the mean transition probability from channel (Z_1, N_1) to (Z_1', N_1) and (Z_1, N_1) to (Z_1, N_1') at time t, respectively. d_{Z_1,N_1} is the microscopic dimension representing the microscopic state number of the fragment for the macroscopic state (Z_1, N_1, E_1) [80]. The dissipation of relative kinetic energy provides the local excitation energy E_1 of the composite system. Λ_{qf} and Λ_{fis} describe the quasifission rate and fission rate of the DNS, respectively, as detailed in the Ref. [75]. Taking the calculation of the mean transition probability of proton transition as an example:

$$\begin{aligned}
&W_{Z_1,N_1;Z_1',N_1}(t) \\
&= \frac{\tau_{\mathrm{mem}}[Z_1, N_1, E_1(Z_1, N_1); Z_1', N_1, E_1(Z_1', N_1)]}{d_{Z_1,N_1}d_{Z_1',N_1}\hbar^2} \\
&\quad \times \sum_{ii'} |\langle Z_1', N_1, E_1(Z_1', N_1), \\
&\quad \times i'|V(t)|Z_1, N_1, E_1(Z_1, N_1), i\rangle|^2.
\end{aligned} \tag{8}$$

It is assumed that only one nucleon is transferred every step, namely $Z_1' = Z_1 \pm 1$ or $N_1' = N_1 \pm 1$. For details on memory time τ_{mem}, see Ref. [81]. The local excitation energy of the DNS can be written as

$$\begin{aligned}
E_1(Z_1, N_1) = E_{\mathrm{diss}} - \frac{M^2}{2\zeta_{\mathrm{int}}} - [U(Z_1, N_1, \theta_1, \theta_2) \\
- U(Z_{\mathrm{p}}, N_{\mathrm{p}}, \theta_1, \theta_2)],
\end{aligned} \tag{9}$$

$M = J\zeta_{\mathrm{int}}/(\zeta_{\mathrm{int}} + \zeta_{\mathrm{rel}})[1 - \exp(-t/\tau_{\mathrm{J}})]$ is the internal angular momentum of the DNS, here angular momentum relaxation time τ_{J} is set to 12×10^{-22} s. The internal moment of inertia marked as $\zeta_{\mathrm{int}} = \zeta_{\mathrm{int}}^1 + \zeta_{\mathrm{int}}^2$, ζ_{int}^1, and ζ_{int}^2 denote the internal moment of inertia of the two fragments, and can be written as $\zeta_{\mathrm{int}}^i = \frac{M_i}{5R_i(\|)}R_i(\perp)[R_i^2(\perp) + R_i^2(\|)]$ $(i = 1, 2)$. M_i is the mass of the fragment i. $R_i(\|) = R_i^0[1 + \beta_2 Y_{20}(0)]$ and $R_i(\perp) = R_i^0[1 + \beta_2 Y_{20}(\pi/2)]$ are the radii of the quadrupole

deformed nucleus along the symmetry axis and perpendicular to the symmetry axis, respectively. $R_i^0 = 1.16A_i^{1/3}$ is the radius of the sphere with the same volume as the fragment i. $\zeta_{\rm rel} = \mu R_{\rm cont}^2$ is the relative motion moment of inertia, μ is the reduced mass of the system, $R_{\rm cont}$ is the position where nucleon transfer takes place discussed in Sec. II A. The energy dissipated, which have a strong and direct impact on the distribution of the fragments, from the relative kinetic energy into the composite system can be determined by

$$E_{\rm diss}(Z_1, N_1, \theta_1, \theta_2, t) = E_{\rm c.m.} - V_{\rm C}(\theta_1, \theta_2) - \frac{\langle J(t)\rangle^2}{2\zeta_{\rm rel}(\theta_1, \theta_2)} - E_{\rm rad}(J, t). \quad (10)$$

The incident energy in the center of mass frame and the Coulomb barrier are expressed with $E_{\rm c.m.}$ and $V_{\rm C}$, respectively. J is relative angular momentum. The average dissipation energy from radial kinetic energy at time t can be calculated by $< E_{\rm rad}(J,t) >= E_{\rm rad}(J,0)\exp(-t/\tau_{\rm r})$. Here the relaxation time of radial kinetic energy $\tau_{\rm r}$ is 2×10^{-22} s, and $E_{\rm rad}(J,0) = E_{\rm c.m.} - V_{\rm C} - \frac{\langle J_i\rangle^2}{2\zeta_{\rm rel}}$ is the initial radial energy of which the quantities correspond to the initial moment $t = 0$.

The evolution process of the mass distribution probability is over when the time reaches the interaction time. Using the deflection function method to get the interaction time $\tau_{\rm int}$ [82]:

$$\tau_{\rm int}(J_i) = \frac{\Delta\theta\zeta_{\rm tot}}{\hbar J_i} + \frac{1}{\kappa}\ln\frac{J_f}{J_i}, \quad (11)$$

where $\Delta\theta$ is the rotational angle of the DNS, J_i and J_f are the initial angular momentum and the final angular momentum, respectively, $\zeta_{\rm tot}$ is the total moment of inertia, and κ is the relaxation constant.

C. The production cross sections

The following equation gives the production cross section of the primary fragment with proton number Z_1 and neutron number N_1:

$$\sigma_{\rm pr}(Z_1, N_1, \theta_1, \theta_2, E_{\rm c.m.}) = \frac{\pi\hbar^2}{2\mu E_{\rm c.m.}}\sum_J (2J+1)\,[P(Z_1, N_1, E_1, \theta_1, \theta_2, t = \tau_{\rm int}) + Y(Z_1, N_1, E_1, \theta_1, \theta_2)], \quad (12)$$

where $Y(Z_1, N_1, E_1, \theta_1, \theta_2)$ is the quasifission yield of the fragment with Z_1 and N_1 and can be expressed as [75]

$$Y(Z_1, N_1, E_1, \theta_1, \theta_2) = \int_0^{\tau_{\rm int}} \Lambda^{\rm qf}_{Z_1,N_1} P(Z_1, N_1, E_1, \theta_1, \theta_2, t)dt. \quad (13)$$

We calculated the charge distributions of the primary reaction fragments with the four particular orientation configurations in the reaction of ^{86}Kr + ^{166}Er at $E_{\rm c.m.} = 464$ MeV, which corresponds to 1.81 times the Bass interaction barrier [84]. Figure 5 is the charge distribution, solid red circles represent the experimental data [83]. The quadrupole deformation of projectile and target are $\beta_2^{(1)} = 0.053$ and $\beta_2^{(2)} = 0.238$, respectively. The tip-to-tip configuration is shown as a black solid line; one can see that the results give a poor description of the experimental data. The theoretical value far below the experimental data with $Z < 30$ and $Z > 45$, while the opposite trend is observed with $30 < Z < 45$. The results of side-to-side configuration, shown by the blue dashed line, give a significantly better description than tip-to-tip configuration. This phenomenon is consistent with the conclusion in Ref. [85], the orientation of the deformed target at contacting configuration has a very significant influence on the compound system fission process. We also give the results of tip-to-side (olive short dotted line) and side-to-tip (orange dash-dotted line) configurations. In Ref. [41], the experimental data was reproduced by a model based on the Langevin-type dynamical equations of motion, the results of the fragments with $Z > 36$ are in perfect agreement with the experimental data. However, the results of the fragments with $Z < 36$ are below the experimental data because of the negative Q values of the corresponding fragments.

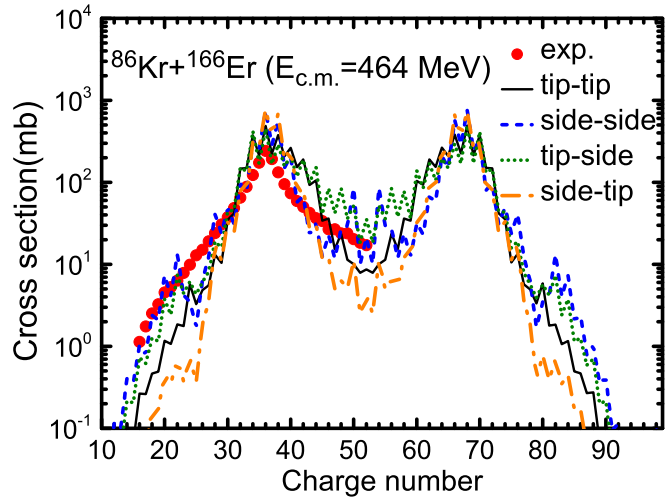

FIG. 5. The charge distributions of the primary reaction fragments in ^{86}Kr + ^{166}Er at $E_{\rm c.m.} = 464$ MeV, the experimental data are taken from Ref. [83] denoted by solid red circles. The quadrupole deformation of ^{86}Kr and ^{166}Er are $\beta_2^{(1)} = 0.053$ and $\beta_2^{(2)} = 0.238$, respectively.

At present, we cannot consider the complex distribution of all possible orientation configurations in our calculations for fully describing various nuclear reactions. At the current theoretical level, taking the average of certain particular orientations is a more effective method to optimize the calculation results. The discussions of various theoretical models on the advantages of averaging in certain orientations can be found in Refs. [42,50,86,87], and the references therein. The average of tip-to-tip and side-to-side configurations and the average of four configurations (tip-to-tip, side-to-side, tip-to-side, and side-to-tip) are showed by the magenta solid and the blue dashed lines in Fig. 6, and marked as av$_{\rm I}$ and av$_{\rm II}$ for convenient description. It is worth mentioning that the two averages are similar to each other, and both can describe the experimental data well. For simplicity, we will take av$_{\rm I}$ as the results of our calculations, which can improve the reliability of theoretical prediction to some extent.

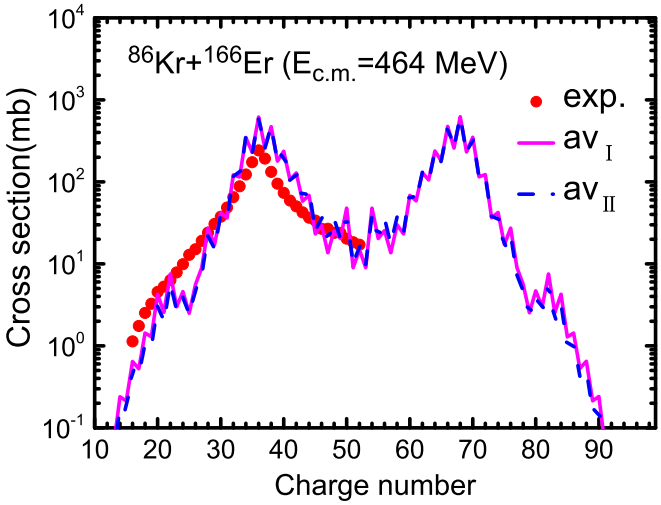

FIG. 6. The same as described in the caption of Fig. 5 but the average results. The experimental data are taken from Ref. [83] denoted by solid red circles. av_I and av_{II} indicate the average of tip-to-tip and side-to-side configurations and the average of four typical configurations (tip-to-tip, side-to-side, tip-to-side, and side-to-tip), respectively.

In conclusion, the reliability of the DNS model has been tested from what has been discussed above. The average of tip-to-tip and side-to-side configurations (av_I) and the average of tip-to-tip, side-to-side, tip-to-side, and side-to-tip configurations (av_{II}) are similar to each other. This work will take av_I as the final result to simplify the calculation in the next section. The statistical model GEMINI is used to deal with the subsequent de-excited process of excited fragments [88]. Except for evaporating γ rays, in principle, the excited fragments can evaporate particles with any mass number during de-excitation. At the same time, the fission process competes with the evaporation process during de-excitation.

III. RESULTS AND DISCUSSION

A. Orientation effects on the PES and interaction time in the ^{204}Hg + ^{232}Th reaction

To produce new neutron-rich isotopes with $Z = 62$–75, this work studied the multinucleon transfer process of ^{204}Hg + ^{232}Th in tip-to-tip and side-to-side configurations (for av_I) based on the DNS model. The transfer process is determined by the shape of the three-dimensional PES, shown in Fig. 7. The red line represents the minimum value in the PES, and the stars indicate the injection points. In the tip-to-tip configuration [see Fig. 7(a)], the PES shows two valleys away from the injection points, it is due to closed sub shells around $Z = 64$, 100 and N = 100, 152, 162. The nucleon transfer process should be in the direction of increasing mass asymmetry under the action of the driving force.

The impact of the shells can be clearly seen in the structure of the driving potential; see Fig. 8. The downward arrows indicate the projectile and the target, the upward arrows indicate the subshells that influenced the transfer process. Figure 7(b) is the three-dimensional PES of side-to-side configuration whose transfer process is a conventional quasifission

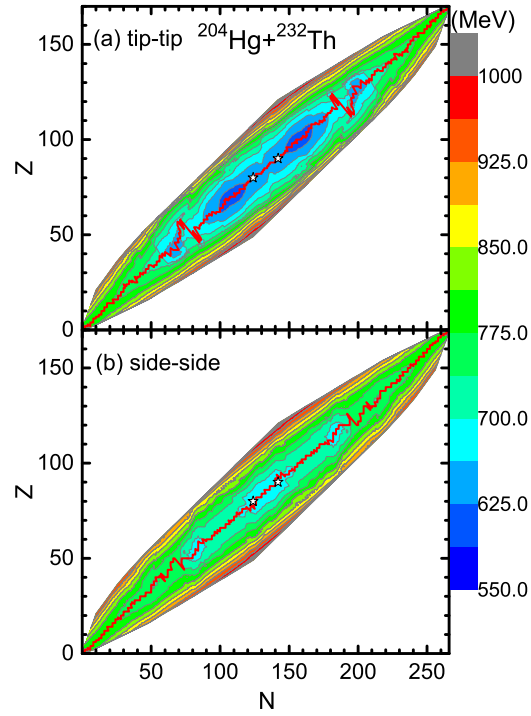

FIG. 7. The potential energy surface (PES) as functions of Z and N of the fragments in ^{204}Hg + ^{232}Th reaction of tip-to-tip (a) and side-to-side (b) configurations, the red line represents the minimum value in the PES, and the stars indicate the injection points.

process. It leads to hardly any production of new neutron-rich isotopes that lighter than the projectile. The corresponding driving potential is shown as the dashed line in Fig. 8. In conclusion, the tip-to-tip configuration accounts for the main contribution to produce new neutron-rich isotopes because of the "inverse" quasifission process in the ^{204}Hg + ^{232}Th reaction. Kozulin and Zagrebaev measured cross sections and

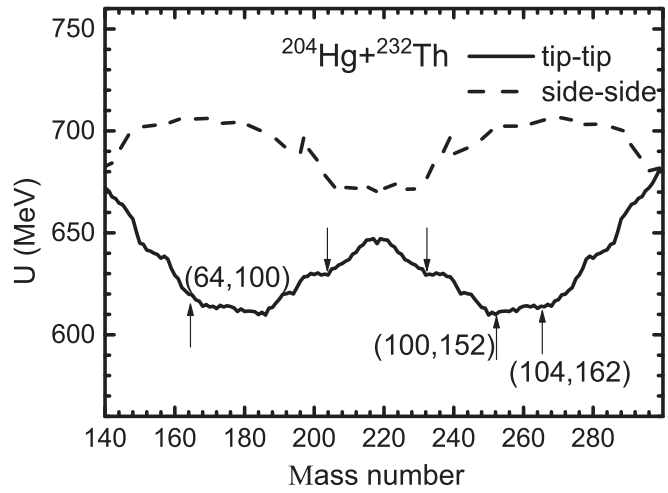

FIG. 8. The driving potential in the reaction of ^{204}Hg + ^{232}Th. The downward arrows indicate the projectile and the target, the upward arrows indicate the sub shells which influenced the transfer process.

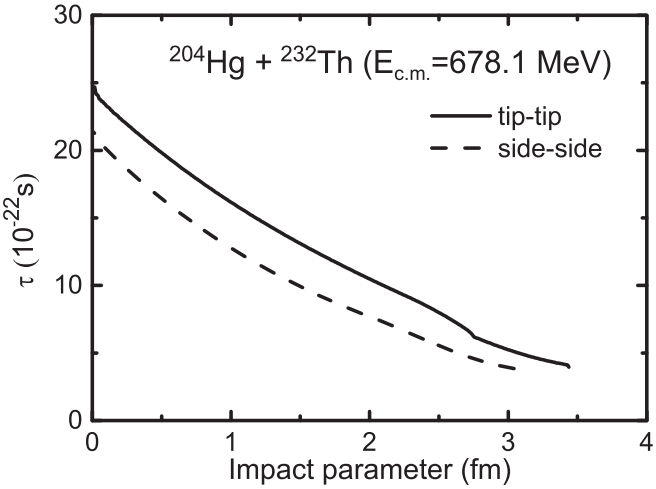

FIG. 9. The interaction time with tip-to-tip (solid line) and side-to-side (dashed line) orientation configurations as a function of the impact parameters in the reactions of $^{204}\mathrm{Hg} + ^{232}\mathrm{Th}$ at $E_{\mathrm{c.m.}} = 1.05V_{\mathrm{C}}$, V_{C} is the Bass interaction barrier [84].

excitation energy in the reactions $^{156,160}\mathrm{Gd} + ^{186}\mathrm{W}$, which exhibit "inverse" quasifission. An enhancement in the yields of trans-target fragments with mass number 200–215 has been found for both reactions. Also, they found that the side-to-side configuration is the "inverse" quasifission process in these two reactions [64].

The ΔU value is calculated by the expression $U(Z_1, N_1, Z_2, N_2) - U(Z_{\mathrm{P}}, N_{\mathrm{P}}, Z_{\mathrm{T}}, N_{\mathrm{T}})$, which represents the potential energy need to be overcome in the transfer process from the entrance channel to the corresponding exit channel. Here, $U(Z_{\mathrm{P}}, N_{\mathrm{P}}, Z_{\mathrm{T}}, N_{\mathrm{T}})$ and $U(Z_1, N_1, Z_2, N_2)$ are the potential energy of the entrance channel and the corresponding exit channel, respectively. In general, the smaller the ΔU value, the larger the production cross sections of the primary products. Based on the three-dimensional PES discussed above, the ΔU values of the tip-to-tip and side-to-side configurations corresponding to new isotopes in $^{204}\mathrm{Hg} + ^{232}\mathrm{Th}$ reaction listed in Table I, marked as ΔU_{tip} and ΔU_{side}, respectively. The corresponding predicted production cross sections of new neutron-rich isotopes at $E_{\mathrm{c.m.}} = 678.1$ MeV, which is 1.05 times the Bass interaction barrier [84], are presented as well. In the tip-to-tip configuration, most of the ΔU values are less than 20 MeV, or even negative values. It means that the primary products have larger production cross sections in this configuration. The ΔU value is -10.63 MeV when the PLF is ^{182}Tm, and the corresponding production cross section is up to 8.30 μb. In the side-to-side configuration, the ΔU values are mostly higher than 20 MeV, so new isotopes are hardly produced in this configuration, as shown in Table I.

In Fig. 9, we present the interaction time as a function of the impact parameters with tip-to-tip (solid line) and side-to-side (dashed line) orientation configurations in the reaction of $^{204}\mathrm{Hg} + ^{232}\mathrm{Th}$ at $E_{\mathrm{c.m.}} = 1.05V_{\mathrm{C}}$. One can see that the interaction time decrease with the increasing of impact parameters. Compared with the side-to-side configuration, the tip-to-tip configuration has a longer interaction time in this reaction because the Coulomb repulsion effects of tip-to-tip configuration are weaker than that of side-to-side configuration. The longer interaction time makes it easier to transfer more nucleons in the tip-to-tip configuration. However, the difference in interaction time between tip-to-tip and side-to-side configurations is not very significant, but the difference in production cross sections are very large, the side-to-side configuration hardly producing any new isotopes. So, compared with the influence of interaction time, the impact of the PES on the cross sections is predominant.

B. Production cross sections of isotopes with $Z = 62$–75 in the $^{204}\mathrm{Hg} + ^{232}\mathrm{Th}$ reaction

The $^{204}\mathrm{Hg} + ^{232}\mathrm{Th}$ reaction gives a significant advantage when producing new neutron-rich isotopes with $Z = 62$–75 due to the "inverse" quasifission process in the tip-to-tip configuration as discussed in Section A. To find the optimal incident energy, the production cross sections of new neutron-rich isotopes in the $^{204}\mathrm{Hg} + ^{232}\mathrm{Th}$ reaction at $E_{\mathrm{c.m.}} = 1.05V_{\mathrm{C}}$ (black solid line), $E_{\mathrm{c.m.}} = 1.10V_{\mathrm{C}}$ (red dashed line), $E_{\mathrm{c.m.}} = 1.15V_{\mathrm{C}}$ (blue dash-dotted line), and $E_{\mathrm{c.m.}} = 1.20V_{\mathrm{C}}$ (olive dash-dot-dotted line) are presented in Figs. 10(a)–10(n). Here, we take $\mathrm{av_I}$ as the final results and only show the results of new isotopes with cross sections larger than 1pb. The experimental data with $Z = 62$–68 are taken from Ref. [4] and the others are taken from Ref. [5] denoted by solid circles, which currently correspond to the most neutron-rich isotopes of relative nuclides. Both experiments measured by using the in-flight fission of ^{238}U beam impinged on the ^{9}Be target at the RIKEN [4] and GSI [5], respectively.

One can see that the production cross sections of most of the isotopes at $E_{\mathrm{c.m.}} = 1.05V_{\mathrm{C}}$ are largest, and of few isotopes appears maximum at $E_{\mathrm{c.m.}} = 1.10V_{\mathrm{C}}$. The predicted production cross sections of the new neutron-rich nuclei ^{179}Ho, ^{181}Er, $^{182-184}$Tm, ^{186}Yb, ^{189}Lu, ^{191,192}Hf, and ^{195}Ta at $E_{\mathrm{c.m.}} = 1.05V_{\mathrm{C}}$, are 0.126 μb, 0.150 μb, 4.15 μb, 7.20 μb, 0.170 μb, 0.555 μb, 0.174 μb, 0.601 μb, 0.169 μb, and 0.118 μb, respectively. The production cross sections in this order of magnitude can be easily detected in MNT reaction experiments. While in the case of $E_{\mathrm{c.m.}} = 1.10V_{\mathrm{C}}$, only the results of ^{177}Dy, ^{182,183}Tm, ^{186}Yb, and ^{191}Hf could be produced in this order of magnitude. And the production cross sections of ^{182,183}Tm, ^{186}Yb, and ^{191}Hf are lower than that of the case $E_{\mathrm{c.m.}} = 1.05V_{\mathrm{C}}$. Overall, $E_{\mathrm{c.m.}} = 1.05V_{\mathrm{C}}$ (678.1 MeV) is more suitable for producing new neutron-rich isotopes with $Z = 62$–75 in the $^{204}\mathrm{Hg} + ^{232}\mathrm{Th}$ reaction, the corresponding cross sections presented in Table I.

From Fig. 10, the production cross sections at $E_{\mathrm{c.m.}} = 1.05V_{\mathrm{C}}$ are 2 to 5 orders of magnitude higher than the experimental data in the projectile fission (PF) reaction. But it should be noted that when comparing the feasibility of experiments, the yields depend not only on the value of the cross sections, but also on the experimental conditions, such as beam intensity, target thickness, and detection efficiency. The significant difference between the two kinds of reaction is the thickness of the target. The target of the PF reaction is about 10 000 times thicker than the MNT reaction [17], which leads to the yields of the former are about 10 000 times

TABLE I. The ΔU values for the tip-to-tip and side-to-side configurations in ^{204}Hg + ^{232}Th. The predicted production cross sections are listed as well. The incident energy takes 1.05 times the Coulomb barrier which is 678.1 MeV.

Isotopes	ΔU_{tip} (MeV)	ΔU_{side} (MeV)	$\sigma_{\text{tip-tip}}$ (μb)	$\sigma_{\text{side-side}}$ (μb)	σ_{av1} (μb)
^{168}Sm	5.61	41.84	1.19×10^{-2}	–	5.93×10^{-3}
^{169}Sm	18.80	46.27	1.53×10^{-5}	–	7.66×10^{-6}
^{170}Eu	6.08	41.76	4.35×10^{-3}	–	2.17×10^{-3}
^{171}Eu	8.16	43.82	1.72×10^{-4}	–	8.60×10^{-5}
^{172}Eu	12.74	48.38	1.52×10^{-5}	–	7.61×10^{-6}
^{172}Gd	0.78	37.07	5.98×10^{-2}	–	2.99×10^{-2}
^{173}Gd	5.03	41.31	1.16×10^{-3}	–	5.82×10^{-4}
^{174}Gd	6.84	43.11	5.23×10^{-4}	–	2.61×10^{-4}
^{175}Gd	10.34	48.17	1.42×10^{-5}	–	7.08×10^{-6}
^{175}Tb	2.19	38.90	1.57×10^{-2}	–	7.83×10^{-3}
^{176}Tb	4.83	43.47	3.03×10^{-3}	–	1.52×10^{-3}
^{177}Tb	6.77	45.39	2.39×10^{-4}	–	1.20×10^{-4}
^{177}Dy	−2.35	37.05	5.90×10^{-2}	–	2.95×10^{-2}
^{178}Dy	−0.19	37.59	6.08×10^{-3}	–	3.04×10^{-3}
^{179}Dy	4.03	41.64	2.01×10^{-3}	–	1.01×10^{-3}
^{180}Dy	6.49	42.63	3.52×10^{-6}	–	1.76×10^{-6}
^{179}Ho	−5.26	34.52	0.251	–	0.126
^{180}Ho	−0.77	37.39	1.38×10^{-2}	–	6.90×10^{-3}
^{181}Ho	0.46	38.58	3.26×10^{-3}	–	1.63×10^{-3}
^{182}Ho	7.80	41.24	1.98×10^{-5}	–	9.93×10^{-6}
^{181}Er	−7.29	31.38	0.300	–	0.150
^{182}Er	−6.73	31.91	0.157	–	7.87×10^{-2}
^{183}Er	0.39	34.31	1.31×10^{-3}	–	6.55×10^{-4}
^{184}Er	4.30	34.92	5.76×10^{-3}	–	2.88×10^{-3}
^{185}Er	11.19	38.49	9.63×10^{-5}	–	4.81×10^{-5}
^{182}Tm	−10.63	28.71	8.30	–	4.15
^{183}Tm	−10.17	28.97	14.4	–	7.20
^{184}Tm	−4.89	31.11	0.340	–	0.170
^{185}Tm	−1.07	31.49	5.13×10^{-2}	–	2.57×10^{-2}
^{186}Tm	5.17	34.37	4.54×10^{-4}	–	2.27×10^{-4}
^{187}Tm	11.52	34.35	4.53×10^{-4}	–	2.27×10^{-4}
^{186}Yb	−6.46	24.84	1.11	–	0.555
^{187}Yb	−0.56	27.37	6.89×10^{-2}	–	3.44×10^{-2}
^{188}Yb	5.02	26.69	1.05×10^{-2}	–	5.27×10^{-3}
^{189}Yb	17.01	44.94	0.117	–	5.83×10^{-2}
^{190}Yb	18.93	45.13	1.22×10^{-4}	–	6.09×10^{-5}
^{189}Lu	1.48	23.30	0.347	–	0.174
^{190}Lu	12.89	41.19	5.42×10^{-2}	–	2.71×10^{-2}
^{191}Lu	14.52	41.09	7.23×10^{-3}	–	3.61×10^{-3}
^{192}Lu	19.67	41.93	2.63×10^{-3}	–	1.32×10^{-3}
^{193}Lu	24.25	40.12	7.24×10^{-6}	–	3.62×10^{-6}
^{191}Hf	7.62	34.55	1.20	–	0.601
^{192}Hf	8.46	33.99	0.337	–	0.169
^{193}Hf	13.34	34.34	1.97×10^{-2}	–	9.85×10^{-3}
^{194}Hf	17.53	30.69	1.30×10^{-2}	–	6.5×10^{-3}
^{195}Hf	22.72	31.26	4.16×10^{-5}	–	2.08×10^{-5}
^{195}Ta	13.71	27.12	0.236	–	0.118
^{196}Ta	18.24	26.99	6.53×10^{-2}	–	3.27×10^{-2}
^{197}Ta	21.62	25.44	7.29×10^{-4}	–	3.64×10^{-4}
^{198}W	15.05	17.61	7.06×10^{-2}	9.72×10^{-6}	3.53×10^{-2}
^{199}W	21.36	14.50	3.17×10^{-3}	1.62×10^{-5}	1.59×10^{-3}
^{200}W	22.78	14.04	2.26×10^{-4}	–	1.13×10^{-4}
^{200}Re	16.53	12.86	5.76×10^{-2}	5.57×10^{-4}	2.91×10^{-2}
^{201}Re	17.50	10.66	8.23×10^{-3}	1.56×10^{-6}	4.12×10^{-3}
^{202}Re	21.36	16.28	4.96×10^{-3}	–	2.48×10^{-3}

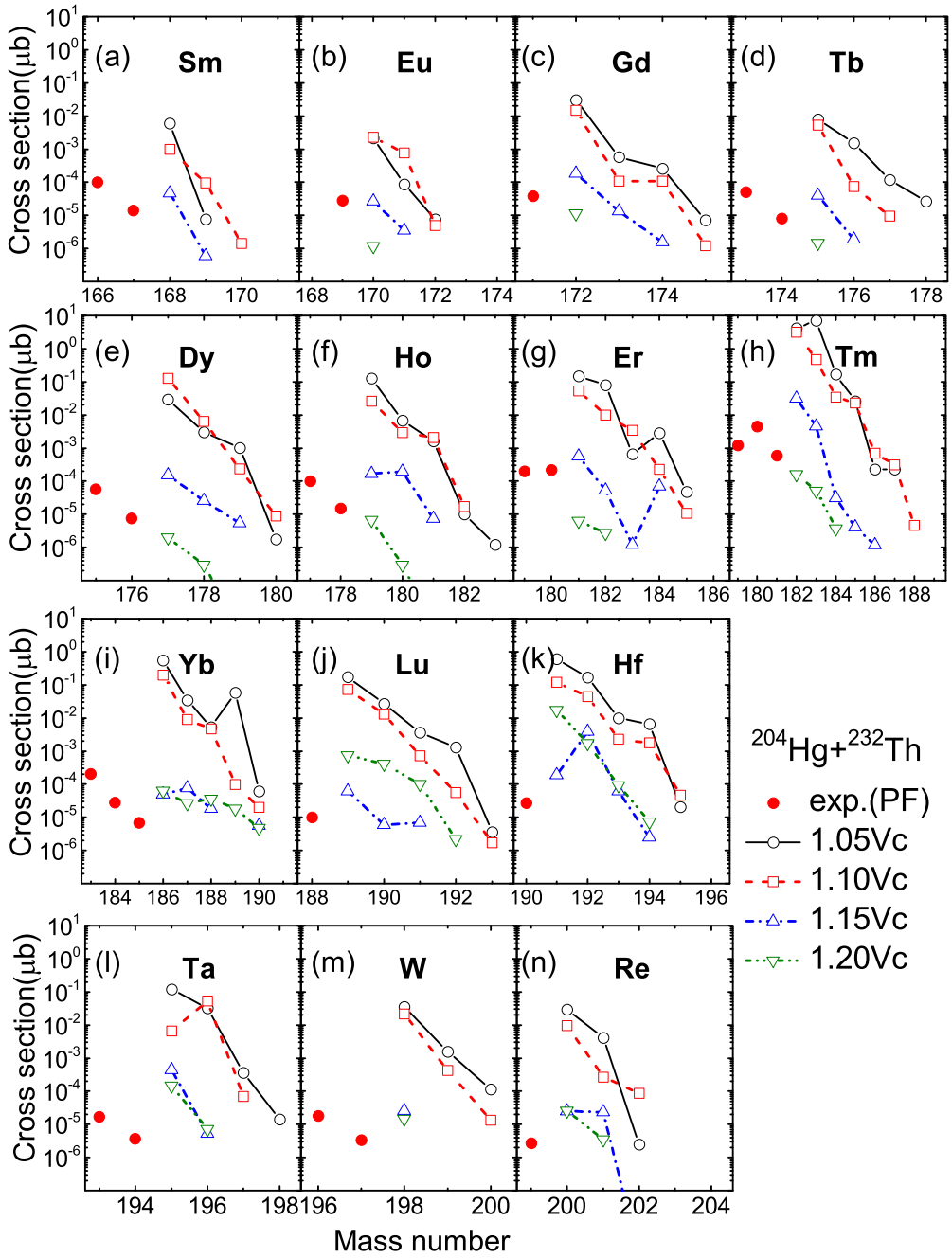

FIG. 10. Final isotopic production cross sections of isotopes with $Z = 62$–75 in the $^{204}\mathrm{Hg} + ^{232}\mathrm{Th}$ reaction at $E_{\mathrm{c.m.}} = 1.05V_{\mathrm{C}}$ (black solid line), $E_{\mathrm{c.m.}} = 1.10V_{\mathrm{C}}$ (red dashed line), $E_{\mathrm{c.m.}} = 1.15V_{\mathrm{C}}$ (blue dash-dotted line), and $E_{\mathrm{c.m.}} = 1.20V_{\mathrm{C}}$ (olive dash-dot-dotted line). The blank symbols denote the new nuclei. The experimental data are taken from Refs. [4] and [5], denoted by solid circles.

higher than that of the latter. Anyway, it is undeniable that the MNT reaction of $^{204}\mathrm{Hg} + ^{232}\mathrm{Th}$ is very competitive to the PF reactions for producing new neutron-rich nuclei with $Z = 62$–75 when considering the advantages of the production cross sections.

C. Production rates of isotopes with $Z = 62$–75 in the $^{204}\mathrm{Hg} + ^{232}\mathrm{Th}$ reaction

We studied the production rate to show the experiment feasibility of the $^{204}\mathrm{Hg} + ^{232}\mathrm{Th}$ reaction at $E_{\mathrm{c.m.}} = 678.1$ MeV. The production rate, which indicates the counts per day, is the crucial standard for comparing the feasibility of experiments. The production rate of the final fragment can be expressed as $N' = \varepsilon\sigma I N_{\mathrm{S}}$. Here, ε is the efficiency of the detection equipment, σ is the production cross section, I is the beam intensity, and N_{S} is the atom number per area of the target. The MNT reaction around the Coulomb barrier of $^{204}\mathrm{Hg} + ^{198}\mathrm{Pt}$ [24] was performed at the ATLAS facility of the Argonne National Laboratory. The beam intensity is 1.3×10^9 particle/s. In the MNT reaction of $^{197}\mathrm{Au} + ^{232}\mathrm{Th}$, the thickness of Th target is 6.3 mg/cm^2 [89]. Hence, it is reasonable to assume that the

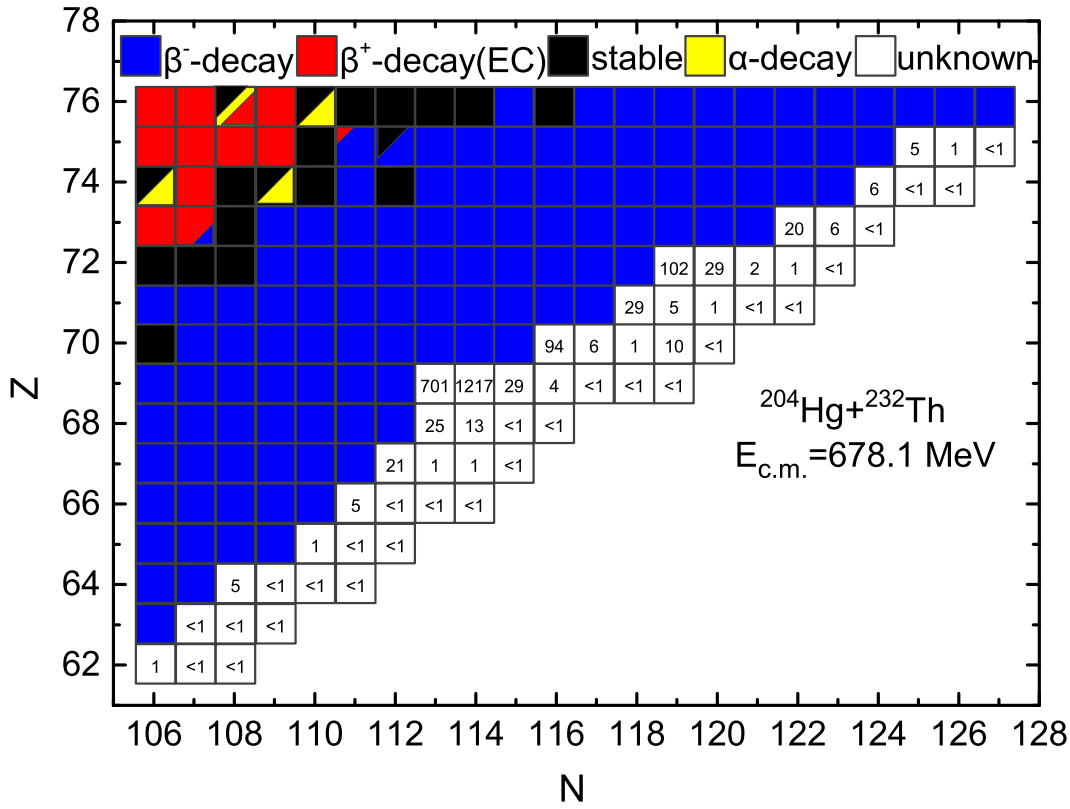

FIG. 11. The nuclei with $Z = 62$–75 on the nuclear map. The filled and open squares denote the known and new nuclei, respectively. Blue, red, black, yellow colors show the β^- decay, β^+ decay, stable, and α decay, respectively. The production rate of new isotopes in the $^{204}\mathrm{Hg} + ^{232}\mathrm{Th}$ reaction at 678.1 MeV are indicated in open squares of the figure, <1 means the counts per day is less than 1. The beam intensity took 1.3×10^9 particle/s produced at the ATLAS facility of the Argonne National Laboratory [24]. The thickness of Th target took 6.3 mg/cm^2 refer to Ref. [89].

beam intensity of ^{204}Hg ions is 1.3×10^9 particle/s and the Th target thickness is 6.3 mg/cm^2. The detection efficiency ε adopts 10%, and σ takes av$_\mathrm{I}$ in our calculation. Figure 11 is a nuclear chart with $Z = 62$–75, the filled and open squares denote the known and new nuclei produced in the present work, respectively. Blue, red, black, yellow colors show the β^- decay, β^+ decay, stable, and α decay, respectively. The production rate of new isotopes in the $^{204}\mathrm{Hg} + ^{232}\mathrm{Th}$ reaction at 678.1 MeV are indicated in open squares of the figure, the symbol <1 represents the counts per day is less than 1. The results are rounded off during the calculation. One can see that 29 new nuclei were produced with production rates more than one count per day. Especially, there are 11 new isotopes whose production rate per day is greater than 10, they are ^{179}Ho (21), ^{181,182}Er (25, 13), ^{182,183,184}Tm (701, 1217, 29), ^{186}Yb (94), ^{189}Lu (29), ^{191,192}Hf (102, 29), and ^{195}Ta (20). In conclusion, a lot of new neutron-rich nuclei with $Z = 62$–75 could be produced in the $^{204}\mathrm{Hg} + ^{232}\mathrm{Th}$ reaction at 678.1 MeV.

IV. CONCLUSIONS

The calculated production cross sections in the $^{86}\mathrm{Kr} + ^{166}\mathrm{Er}$ reaction using the DNS model reproduce the available experimental data well. In the region of $A_1 = 52$–200, the Coulomb potential is the main factor responsible for the differences in the driving potential between different orientation configurations in $^{86}\mathrm{Kr} + ^{166}\mathrm{Er}$. The contribution of the nuclear potential to these differences increases when $A_1 < 52$ and $A_1 > 200$. It can improve the reliability of the prediction to some extent by averaging the results of tip-to-tip and side-to-side orientation configurations as the final results.

The orientation effects on the potential energy surface (PES) and the interaction time in the reaction of $^{204}\mathrm{Hg} + ^{232}\mathrm{Th}$ at $E_{\mathrm{c.m.}} = 1.05V_\mathrm{C}$ are studied. The tip-to-tip configuration has a longer interaction time than that of the side-to-side configuration. The production cross sections are influenced both by the interaction time and by the PES simultaneously, and the influence of the PES on the cross sections is predominant. In this reaction, the tip-to-tip configuration accounts for the main contribution to produce new neutron-rich isotopes because of the "inverse" quasifission process.

This work predicted the production cross sections of new neutron-rich isotopes with $Z = 62$–75 in the reaction of $^{204}\mathrm{Hg} + ^{232}\mathrm{Th}$. $E_{\mathrm{c.m.}} = 1.05V_\mathrm{C}$ (i.e., 678.1 MeV) is the suitable energy. Most of the calculated cross sections predicted here are two to five orders of magnitude higher than the cross sections of the most neutron-rich isotopes of relative nuclides measured in the projectile fission (PF) experiments.

Considering the experimental conditions (beam intensity, target thickness, and detection efficiency) provided by the experiments, the production rates for the synthesis of the new isotopes ^{179}Ho, ^{181,182}Er, ^{182,183,184}Tm, ^{186}Yb, ^{189}Lu, ^{191,192}Hf, and ^{195}Ta are 21, 25, 13, 701, 1217, 29, 94, 29, 102, 29, and 20, respectively. It is very promising to produce new neutron-rich isotopes with $Z = 62$–75 in the $^{204}\mathrm{Hg} + {}^{232}\mathrm{Th}$ reaction at 678.1 MeV in the future.

ACKNOWLEDGMENTS

This work was supported by the National Natural Science Foundation of China under Grants No. 11635003, No. 11961141004, No. 11025524, No. 11161130520, and No. 12047513; the National Basic Research Program of China under Grant No. 2010CB832903; the European Commissions 7th Framework Programme (Fp7-PEOPLE-2010-IRSES) under Grant No. 269131.

[1] https://people.nscl.msu.edu/~thoennes/isotopes (2020).
[2] M. R. Mumpower, R. Surman, G. McLaughlin, and A. Aprahamian, Prog. Part. Nucl. Phys. **86**, 126 (2016).
[3] Y. X. Watanabe, Y. H. Kim, S. C. Jeong, Y. Hirayama, N. Imai, H. Ishiyama, H. S. Jung, H. Miyatake, S. Choi, J. S. Song, E. Clement, G. de France, A. Navin, M. Rejmund, C. Schmitt, G. Pollarolo, L. Corradi, E. Fioretto, D. Montanari, M. Niikura, D. Suzuki, H. Nishibata, and J. Takatsu, Phys. Rev. Lett. **115**, 172503 (2015).
[4] N. Fukuda, T. Kubo, D. Kameda, N. Inabe, H. Suzuki, Y. Shimizu, H. Takeda, K. Kusaka, Y. Yanagisawa, M. Ohtake, H. Suzuki, and Y. Shimizu, J. Phys. Soc. Jpn. **87**, 014202 (2018).
[5] J. Kurcewicz, F. Farinon, H. Geissel, S. Pietri, C. Nociforo, A. Prochazka, H. Weick, J. Winfield, A. Estradé, P. Allegro, A. Bail, G. Bélier, J. Benlliure, G. Benzoni, M. Bunce, M. Bowry, R. Caballero-Folch, I. Dillmann, A. Evdokimov, J. Gerl, A. Gottardo, E. Gregor, R. Janik, A. Kelić-Heil, R. Knöbel, T. Kubo, Y. Litvinov, E. Merchan, I. Mukha, F. Naqvi, M. Pfützner, M. Pomorski, Z. Podolyák, P. Regan, B. Riese, M. Ricciardi, C. Scheidenberger, B. Sitar, P. Spiller, J. Stadlmann, P. Strmen, B. Sun, I. Szarka, J. Taïeb, S. Terashima, J. Valiente-Dobón, M. Winkler, and P. Woods, Phys. Lett. B **717**, 371 (2012).
[6] E. Runte, W. D. Schmidt-Ott, W. Eschner, I. Rosner, R. Kirchner, O. Klepper, and K. Rykaczewski, Z. Phys. A **328**, 119 (1987).
[7] R. M. Chasteler, J. M. Nitschke, R. B. Firestone, K. S. Vierinen, P. A. Wilmarth, and A. A. Shihab-Eldin, Z. Phys. A: Hadrons Nucl. **332**, 239 (1989).
[8] K. Becker, F. Meissner, W. D. Schmidt-Ott, U. Bosch, V. Kunze, H. Salewski, R. Kirchner, O. Klepper, E. Roeckl, D. Schardt, and K. Rykaczewski, Nucl. Phys. A **522**, 557 (1991).
[9] P. A. Söderström, J. Nyberg, P. H. Regan, A. Algora, G. de Angelis, S. F. Ashley, S. Aydin, D. Bazzacco, R. J. Casperson, W. N. Catford, J. Cederkäll, R. Chapman, L. Corradi, C. Fahlander, E. Farnea, E. Fioretto, S. J. Freeman, A. Gadea, W. Gelletly, A. Gottardo, E. Grodner, C. Y. He, G. A. Jones, K. Keyes, M. Labiche, X. Liang, Z. Liu, S. Lunardi, N. Mărginean, P. Mason, R. Menegazzo, D. Mengoni, G. Montagnoli, D. Napoli, J. Ollier, S. Pietri, Z. Podolyák, G. Pollarolo, F. Recchia, E. Şahin, F. Scarlassara, R. Silvestri, J. F. Smith, K. M. Spohr, S. J. Steer, A. M. Stefanini, S. Szilner, N. J. Thompson, G. M. Tveten, C. A. Ur, J. J. Valiente-Dobón, V. Werner, S. J. Williams, F. R. Xu, and J. Y. Zhu, Phys. Rev. C **81**, 034310 (2010).
[10] L. Corradi, A. M. Vinodkumar, A. M. Stefanini, E. Fioretto, G. Prete, S. Beghini, G. Montagnoli, F. Scarlassara, G. Pollarolo, F. Cerutti, and A. Winther, Phys. Rev. C **66**, 024606 (2002).
[11] W. Królas, R. Broda, B. Fornal, T. Pawłat, J. Wrzesiński, D. Bazzacco, G. de Angelis, S. Lunardi, R. Menegazzo, D. R. Napoli, and C. Rossi Alvarez, Nucl. Phys. A **832**, 170 (2010).
[12] L. X. Chen, W. R. Plass, H. Geissel, R. Knöbel, C. Kozhuharov, Y. A. Litvinov, Z. Patyk, C. Scheidenberger, K. Siegień-Iwaniuk, B. Sun,, H. Weick, K. Beckert, P. Beller, F. Bosch, D. Boutin, L. Caceres, J. Carroll, D. Cullen, I. J. Cullen, B. Franzke, J. Gerl, M. Górska, G. A. Jones, A. Kishada, J. Kurcewicz, S. A. Litvinov, Z. Liu, S. Mandal, F. Montes, G. Münzenberg, F. Nolden, T. Ohtsubo, Z. Podolyák, R. Propri, S. Rigby, N. Saito, T. Saito, M. Shindo, M. Steck, P. Ugorowski, P. M. Walker, S. Williams, M. Winkler, H. J. Wollersheim, and T. Yamaguchi, Phys. Lett. B **691**, 234 (2010).
[13] W. Loveland, A. M. Vinodkumar, D. Peterson, and J. P. Greene, Phys. Rev. C **83**, 044610 (2011).
[14] E. M. Kozulin, E. Vardaci, G. N. Knyazheva, A. A. Bogachev, S. N. Dmitriev, I. M. Itkis, M. G. Itkis, A. G. Knyazev, T. A. Loktev, K. V. Novikov, E. A. Razinkov, O. V. Rudakov, S. V. Smirnov, W. Trzaska, and V. I. Zagrebaev, Phys. Rev. C **86**, 044611 (2012).
[15] J. V. Kratz, M. Schädel, and H. W. Gäggeler, Phys. Rev. C **88**, 054615 (2013).
[16] E. M. Kozulin, G. N. Knyazheva, S. N. Dmitriev, I. M. Itkis, M. G. Itkis, T. A. Loktev, K. V. Novikov, A. N. Baranov, W. H. Trzaska, E. Vardaci, S. Heinz, O. Beliuskina, and S. V. Khlebnikov, Phys. Rev. C **89**, 014614 (2014).
[17] O. Beliuskina, S. Heinz, V. Zagrebaev, V. Comas, C. Heinz, S. Hofmann, R. Knöbel, M. Stahl, D. Ackermann, F. P. Heßberger, B. Kindler, B. Lommel, J. Maurer, and R. Mann, Eur. Phys. J. A **50**, 161 (2014).
[18] S. Heinz, O. Beliuskina, V. Comas, H. M. Devaraja, C. Heinz, S. Hofmann, E. Kozulin, F. Morherr, G. Münzenberg, D. Ackermann, F. P. Heßberger, B. Kindler, B. Lommel, R. Mann, and J. Maurer, Eur. Phys. J. A **51**, 140 (2015).
[19] H. M. Devaraja, S. Heinz, O. Beliuskina, V. Comas, S. Hofmann, C. Hornung, G. Münzenberg, K. Nishio, D. Ackermann, Y. K. Gambhir, M. Gupta, R. A. Henderson, F. P. Heßberger, J. Khuyagbaatar, B. Kindler, B. Lommel, K. J. Moody, J. Maurer, R. Mann, A. G. Popeko, D. A. Shaughnessy, M. A. Stoyer, and A. V. Yeremin, Phys. Lett. B **748**, 199 (2015).
[20] A. Vogt, B. Birkenbach, P. Reiter, L. Corradi, T. Mijatović, D. Montanari, S. Szilner, D. Bazzacco, M. Bowry, A. Bracco, B. Bruyneel, F. C. L. Crespi, G. de Angelis, P. Désesquelles, J. Eberth, E. Farnea, E. Fioretto, A. Gadea, K. Geibel, A. Gengelbach, A. Giaz, A. Görgen, A. Gottardo, J. Grebosz, H. Hess, P. R. John, J. Jolie, D. S. Judson, A. Jungclaus, W. Korten, S. Leoni, S. Lunardi, R. Menegazzo, D. Mengoni, C. Michelagnoli, G. Montagnoli, D. Napoli, L. Pellegri, G. Pollarolo, A. Pullia, B. Quintana, F. Radeck, F. Recchia, D.

Rosso, E. Şahin, M. D. Salsac, F. Scarlassara, P. A. Söderström, A. M. Stefanini, T. Steinbach, O. Stezowski, B. Szpak, C. Theisen, C. Ur, J. J. Valiente-Dobón, V. Vandone, and A. Wiens, Phys. Rev. C **92**, 024619 (2015).

[21] M. Varga Pajtler, S. Szilner, L. Corradi, G. de Angelis, E. Fioretto, A. Gadea, F. Haas, S. Lunardi, D. Jelavić Malenica, N. Mărginean, D. Mengoni, T. Mijatović, G. Montagnoli, D. Montanari, G. Pollarolo, F. Recchia, M. D. Salsac, F. Scarlassara, N. Soić, A. M. Stefanini, C. A. Ur, and J. J. Valiente-Dobón, Nucl. Phys. A **941**, 273 (2015).

[22] J. S. Barrett, W. Loveland, R. Yanez, S. Zhu, A. D. Ayangeakaa, M. P. Carpenter, J. P. Greene, R. V. F. Janssens, T. Lauritsen, E. A. McCutchan, A. A. Sonzogni, C. J. Chiara, J. L. Harker, and W. B. Walters, Phys. Rev. C **91**, 064615 (2015).

[23] S. Heinz, H. M. Devaraja, O. Beliuskina, V. Comas, S. Hofmann, C. Hornung, G. Münzenberg, D. Ackermann, M. Gupta, R. A. Henderson, F. P. Heßberger, B. Kindler, B. Lommel, R. Mann, J. Maurer, K. J. Moody, K. Nishio, A. G. Popeko, D. A. Shaughnessy, M. A. Stoyer, and A. V. Yeremin, Eur. Phys. J. A **52**, 278 (2016).

[24] T. Welsh, W. Loveland, R. Yanez, J. Barrett, E. McCutchan, A. Sonzogni, T. Johnson, S. Zhu, J. Greene, A. Ayangeakaa, M. Carpenter, T. Lauritsen, J. Harker, W. Walters, B. Amro, and P. Copp, Phys. Lett. B **771**, 119 (2017).

[25] F. Galtarossa, L. Corradi, S. Szilner, E. Fioretto, G. Pollarolo, T. Mijatovic, D. Montanari, D. Ackermann, D. Bourgin, S. Courtin, G. Fruet, A. Goasduff, J. Grebosz, F. Haas, D. Jelavic Malenica, S. C. Jeong, H. M. Jia, P. R. John, D. Mengoni, M. Milin, G. Montagnoli, F. Scarlassara, N. Skukan, N. Soic, A. M. Stefanini, E. Strano, V. Tokic, C. A. Ur, J. J. Valiente-Dobón, and Y. X. Watanabe, CERN Proc. **1**, 89 (2019).

[26] V. V. Desai, W. Loveland, K. McCaleb, R. Yanez, G. Lane, S. S. Hota, M. W. Reed, H. Watanabe, S. Zhu, K. Auranen, A. D. Ayangeakaa, M. P. Carpenter, J. P. Greene, F. G. Kondev, D. Seweryniak, R. V. F. Janssens, and P. A. Copp, Phys. Rev. C **99**, 044604 (2019).

[27] H. M. Devaraja, S. Heinz, O. Beliuskina, S. Hofmann, C. Hornung, G. Münzenberg, D. Ackermann, M. Gupta, Y. K. Gambhir, R. A. Henderson, F. P. Heßberger, A. V. Yeremin, B. Kindler, B. Lommel, J. Maurer, K. J. Moody, K. Nishio, A. G. Popeko, M. A. Stoyer, and D. A. Shaughnessy, Eur. Phys. J. A **55**, 1 (2019).

[28] H. M. Devaraja, S. Heinz, D. Ackermann, T. Göbel, F. P. Heßberger, S. Hofmann, J. Maurer, G. Münzenberg, A. G. Popeko, and A. V. Yeremin, Eur. Phys. J. A **56**, 1 (2020).

[29] V. V. Desai, A. Pica, W. Loveland, J. S. Barrett, E. A. McCutchan, S. Zhu, A. D. Ayangeakaa, M. P. Carpenter, J. P. Greene, T. Lauritsen, R. V. F. Janssens, B. M. S. Amro, and W. B. Walters, Phys. Rev. C **101**, 034612 (2020).

[30] N. V. Antonenko, E. A. Cherepanov, A. K. Nasirov, V. P. Permjakov, and V. V. Volkov, Phys. Lett. B **319**, 425 (1993).

[31] G. G. Adamian, R. V. Jolos, A. K. Nasirov, and A. I. Muminov, Phys. Rev. C **53**, 871 (1996).

[32] A. Nasirov, G. Giardina, G. Mandaglio, M. Manganaro, and A. Muminov, Int. J. Mod Phys E **19**, 997 (2010).

[33] Z. Q. Feng, Phys. Rev. C **95**, 024615 (2017).

[34] L. Zhu, P. W. Wen, C. J. Lin, X. J. Bao, J. Su, C. Li, and C. C. Guo, Phys. Rev. C **97**, 044614 (2018).

[35] G. Zhang, C. A. T. Sokhna, Z. Liu, and F. S. Zhang, Phys. Rev. C **100**, 024613 (2019).

[36] R. Yanez and W. Loveland, Phys. Rev. C **91**, 044608 (2015).

[37] A. Winther, Nucl. Phys. A **572**, 191 (1994).

[38] A. Winther, Nucl. Phys. A **594**, 203 (1995).

[39] P. W. Wen, C. J. Lin, C. Li, L. Zhu, F. Zhang, F. S. Zhang, H. M. Jia, F. Yang, N. R. Ma, L. J. Sun, D. X. Wang, F. P. Zhong, H. H. Sun, L. Yang, and X. X. Xu, Phys. Rev. C **99**, 034606 (2019).

[40] V. I. Zagrebaev, Y. Aritomo, M. G. Itkis, Y. T. Oganessian, and M. Ohta, Phys. Rev. C **65**, 014607 (2001).

[41] V. I. Zagrebaev and W. Greiner, Phys. Rev. C **87**, 034608 (2013).

[42] V. V. Saiko and A. V. Karpov, Phys. Rev. C **99**, 014613 (2019).

[43] S. Ayik, Phys. Lett. B **658**, 174 (2008).

[44] K. Sekizawa and K. Yabana, Phys. Rev. C **88**, 014614 (2013).

[45] S. Ayik, B. Yilmaz, and O. Yilmaz, Phys. Rev. C **92**, 064615 (2015).

[46] S. Ayik, O. Yilmaz, B. Yilmaz, A. S. Umar, A. Gokalp, G. Turan, and D. Lacroix, Phys. Rev. C **91**, 054601 (2015).

[47] K. Sekizawa and K. Yabana, Phys. Rev. C **93**, 054616 (2016).

[48] S. Ayik, B. Yilmaz, O. Yilmaz, and A. S. Umar, Phys. Rev. C **97**, 054618 (2018).

[49] S. Ayik, B. Yilmaz, O. Yilmaz, and A. S. Umar, Phys. Rev. C **100**, 014609 (2019).

[50] Z. J. Wu and L. Guo, Phys. Rev. C **100**, 014612 (2019).

[51] N. Wang and L. Guo, Phys. Lett. B **760**, 236 (2016).

[52] K. Zhao, Z. Li, N. Wang, Y. Zhang, Q. Li, Y. Wang, and X. Wu, Phys. Rev. C **92**, 024613 (2015).

[53] C. Li, X. X. Xu, J. J. Li, G. Zhang, B. Li, C. A. Sokhna, Z. S. Ge, F. Zhang, P. W. Wen, and F. S. Zhang, Phys. Rev. C **99**, 024602 (2019).

[54] L. Corradi, G. Pollarolo, and S. Szilner, J. Phys. G **36**, 113101 (2009).

[55] J. V. Kratz, W. Loveland, and K. J. Moody, Nucl. Phys. A **944**, 117 (2015).

[56] F. S. Zhang, C. Li, L. Zhu, and P. W. Wen, Front. Phys. **13**, 132113 (2018).

[57] W. D. Loveland, Front. Phys. **7**, 23 (2019).

[58] G. G. Adamian, N. V. Antonenko, A. Diaz-Torres, and S. Heinz, Eur. Phys. J. A **56**, 1 (2020).

[59] K. Washiyama and K. Sekizawa, Front. Phys. **8**, 93 (2020).

[60] L. Zhu, C. Li, C. C. Guo, J. Su, P. W. Wen, G. Zhang, and F. S. Zhang, Int. J. Mod. Phys. E **29**, 2030004 (2020).

[61] V. I. Zagrebaev, Y. T. Oganessian, M. G. Itkis, and W. Greiner, Phys. Rev. C **73**, 031602(R) (2006).

[62] V. Zagrebaev and W. Greiner, J. Phys. G: Nucl. Part. Phys. **34**, 2265 (2007).

[63] V. I. Zagrebaev and W. Greiner, Phys. Rev. C **83**, 044618 (2011).

[64] E. M. Kozulin, V. I. Zagrebaev, G. N. Knyazheva, I. M. Itkis, K. V. Novikov, M. G. Itkis, S. N. Dmitriev, I. M. Harca, A. E. Bondarchenko, A. V. Karpov, V. V. Saiko, and E. Vardaci, Phys. Rev. C **96**, 064621 (2017).

[65] D. J. Hinde, M. Dasgupta, J. R. Leigh, J. P. Lestone, J. C. Mein, C. R. Morton, J. O. Newton, and H. Timmers, Phys. Rev. Lett. **74**, 1295 (1995).

[66] M. G. Itkis, J. Äystö, S. Beghini, A. A. Bogachev, L. Corradi, O. Dorvaux, A. Gadea, G. Giardina, F. Hanappe, I. M. Itkis, M. Jandel, J. Kliman, S. V. Khlebnikov, G. N. Kniajeva, N. A. Kondratiev, E. M. Kozulin, L. Krupa, A. Latina, T. Materna, G. Montagnoli, Y. T. Oganessian, I. V. Pokrovsky, E. V. Prokhorova, N. Rowley, V. A. Rubchenya, A. Y. Rusanov, R. N. Sagaidak, F. Scarlassara, A. M. Stefanini, L. Stuttge, S. Szilner, M. Trotta, W. H. Trzaska, D. N. Vakhtin, A. M.

Vinodkumar, V. M. Voskressenski, and V. I. Zagrebaev, Nucl. Phys. A **734**, 136 (2004).
[67] E. M. Kozulin, G. N. Knyazheva, I. M. Itkis, M. G. Itkis, A. A. Bogachev, E. V. Chernysheva, L. Krupa, F. Hanappe, O. Dorvaux, L. Stuttgé, W. H. Trzaska, C. Schmitt, and G. Chubarian, Phys. Rev. C **90**, 054608 (2014).
[68] W. J. Swiatecki, Phys. Scr. **24**, 113 (1981).
[69] L. Zhu, J. Su, P. W. Wen, C. C. Guo, and C. Li, Phys. Rev. C **98**, 034609 (2018).
[70] K. Godbey, A. S. Umar, and C. Simenel, Phys. Rev. C **100**, 024610 (2019).
[71] G. G. Adamian, N. V. Antonenko, and W. Scheid, Nucl. Phys. A **618**, 176 (1997).
[72] G. G. Adamian, N. V. Antonenko, W. Scheid, and V. V. Volkov, Nucl. Phys. A **633**, 409 (1998).
[73] P. Möller, J. Nix, W. Myers, and W. Swiatecki, At. Data Nucl. Data Tables **59**, 185 (1995).
[74] C. Y. Wong, Phys. Rev. Lett. **31**, 766 (1973).
[75] G. G. Adamian, N. V. Antonenko, and W. Scheid, Phys. Rev. C **68**, 034601 (2003).
[76] A. B. Migdal, *Theory of Finite Fermi Systems and Applications to Atomic Nuclei* (Interscience, New York, 1967).
[77] R. A. Gherghescu, Phys. Rev. C **67**, 014309 (2003).
[78] R. A. Gherghescu, W. Greiner, and G. Münzenberg, Phys. Rev. C **68**, 054314 (2003).
[79] L. Zhu, F. S. Zhang, P. W. Wen, J. Su, and W. J. Xie, Phys. Rev. C **96**, 024606 (2017).
[80] S. Ayik, B. Schürmann, and W. Nörenberg, Z. Phys. A: Atoms Nucl. **277**, 299 (1976).
[81] J. Q. Li, X. T. Tang, and G. Wolschin, Phys. Lett. B **105**, 107 (1981).
[82] G. Wolschin and W. Nörenberg, Z. Phys. A: Atoms Nucl. **284**, 209 (1978).
[83] A. Gobbi, U. Lynen, A. Olmi, G. Rudolf, and H. Sann, in *Proceedings of the International School of Physics "Enrico Fermi," Course LXXVII, Varenna on Lake Como, Villa Monastero, 9th–21st July 1979* (North–Holland, Amsterdam, 1981).
[84] R. Bass, Phys. Rev. Lett. **39**, 265 (1977).
[85] D. J. Hinde, M. Dasgupta, J. R. Leigh, J. C. Mein, C. R. Morton, J. O. Newton, and H. Timmers, Phys. Rev. C **53**, 1290 (1996).
[86] S. Q. Guo, X. J. Bao, H. F. Zhang, J. Q. Li, and N. Wang, Phys. Rev. C **100**, 054616 (2019).
[87] L. Zhu, Z. Q. Feng, C. Li, and F. S. Zhang, Phys. Rev. C **90**, 014612 (2014).
[88] R. J. Charity, M. A. McMahan, G. J. Wozniak, R. J. McDonald, L. G. Moretto, D. G. Sarantites, L. G. Sobotka, G. Guarino, A. Pantaleo, L. Fiore, A. Gobbi, and K. D. Hildenbrand, Nucl. Phys. A **483**, 371 (1988).
[89] M. Barbui, T. Materna, P. Sahu, A. Wieloch, F. D. Becchetti, G. Chubaryan, M. Cinausero, T. W. O'donnell, D. Fabris, H. Griffin, K. Hagfl, S. Kowalski, M. Lunardon, Z. Majka, S. Moretto, R. Murthy, J. B. Natowitz, G. Nebbia, S. Pesente, G. Prete, L. Qin, V. Rizzi, Z. Sosin, G. Souliotis, G. Viesti, R. Wada, and J. Wang, Int. J. Mod. Phys. E **18**, 1036 (2009).